OPTICA

Dual-oscillator infrared electro-optic sampling with attosecond precision

Alexander Weigel,[1,2,3,8,†] Philip Jacob,[1,2,†] Wolfgang Schweinberger,[1,2,3] Marinus Huber,[1] Michael Trubetskov,[1] Patrik Karandušovský,[3] Christina Hofer,[1,2,3] Theresa Buberl,[1,2] Tatiana Amotchkina,[1] Maximilian Högner,[1] Daniel Hahner,[2] Philipp Sulzer,[4] Alfred Leitenstorfer,[4] Vladimir Pervak,[2] Ferenc Krausz,[1,2,3] and Ioachim Pupeza[1,2,5,6,7,*]

[1]Max Planck Institute of Quantum Optics, Hans-Kopfermann-Str. 1, 85748 Garching, Germany
[2]Ludwig-Maximilians-Universität München, Am Coulombwall 1, 85748 Garching, Germany
[3]Center for Molecular Fingerprinting (CMF), 1093 Budapest, Czuczor Utca 2-10, Hungary
[4]Department of Physics and Center for Applied Photonics, University of Konstanz, 78457 Konstanz, Germany
[5]Leibniz Institute of Photonic Technology-Member of the research alliance "Leibniz Health Technologies", Albert-Einstein-Straße 9, 07745 Jena, Germany
[6]Cluster of Excellence Balance of the Microverse, Friedrich Schiller University Jena, Jena, Germany
[7]Physics Department and State Research Center OPTIMAS, University of Kaiserslautern-Landau, 67663 Kaiserslautern, Germany
[8]alexander.weigel@mpq.mpg.de
[†]These authors contributed equally to this work.
*ioachim.pupeza@mpq.mpg.de

Received 11 December 2023; revised 24 March 2024; accepted 27 March 2024; published 20 May 2024

Electro-optic sampling of infrared electric fields has set sensitivity and dynamic-range records in broadband molecular vibrational spectroscopy. Yet, in these works, the 1-second-scale single-trace acquisition time leads to intra-scan noise accumulation and restricts the throughput in measurements of multiple samples and of dynamic processes. We present a dual-laser-oscillator approach capturing 2800 mid-infrared waveforms per second by scanning the relative delay between the sampled waveform and the gate pulses using a modulated repetition-frequency lock. The new technique of electro-optic delay tracking (EODT) provides delay calibration with down to few-attosecond precision and provides a general route to high-precision dual-oscillator spectroscopy with picosecond delay ranges. Our work has immediate applications in, e.g., precision electric-field metrology and high-speed biosensing.

https://doi.org/10.1364/OPTICA.515708

1. INTRODUCTION

Infrared (IR) spectroscopy informs on the molecular structure and composition of a sample by probing the resonant vibrational response of molecules, making it a widely used analytical technique in physics, chemistry, and biology. Its potential for medical diagnostics has also been showcased in multiple studies by probing human blood serum or plasma [1–4], urine [5], bile [6], sputum [7,8], saliva [9,10], and breath [11] for disease detection. Moreover, the high temporal stability of the IR molecular fingerprint of human blood serum and plasma opens a potential pathway towards personalized health monitoring [12].

Traditionally, Fourier-transform IR (FTIR) spectroscopy has been used as the standard technique for broadband vibrational spectroscopy of complex biological systems [13]. Recent advances in ultrafast laser technology have led to powerful, waveform-stable few-cycle mid-IR pulses, with their electric-field evolution captured [14,15] with sensitivities approaching the single-photon level [16]. When exciting a molecular sample with these pulses, the molecules coherently re-emit a portion of the energy absorbed at vibrational resonances as picosecond-scale mid-IR radiation in the wake of the femtosecond excitation pulse [17,18]. Sampling the electric-field waveform directly monitors this process [18] and separates the weak molecular response from the strong excitation and its technical noise, offering improved sensitivity as compared to time-integrating measurements [17,19,20].

Field-sensitive detection further benefits from the square-root-relationship of the signal with respect to mid-IR intensity, intrinsically increasing the achievable measurement dynamic range and maximum sample thickness compared to detectors yielding signals that scale with intensity [17,21]. As a common technique for field-sensitive detection, electro-optic sampling (EOS) overlaps the mid-IR waveform with a femtosecond gate pulse and measures the change in gate-pulse polarization induced by the mid-IR electric field [17,22–25]. The near-IR gate pulses further benefit sensitivity by allowing the use of low-noise near-IR detectors instead of their noisier and costlier mid-IR counterparts.

Improved sensitivity not only allows weaker effects to be observed but can also be used to increase acquisition speed.

High-speed field-sensitive IR spectroscopy with sub-millisecond acquisition times has various potential applications, including the time-resolved interrogation of reaction kinetics [26–28], protein conformational changes [29], and breath gases [30], as well as label-free flow cytometry [31–33]. The acquisition of electric-field waveforms at multi-kHz rates allows the elimination of sub-kHz technical noise contributions from mechanical vibrations, laser drifts, and electrically induced fluctuations during the acquisition of a single waveform. Their averaging from repeated measurements can then substantially improve the sensitivity and precision for the measured waveform [34].

Scanning over delay ranges of several picoseconds, as needed for condensed-phase spectroscopy, has traditionally been realized with a calibrated mechanical translation stage moving a retroreflector. This limits delay scan rates to a few Hertz. Increasing acquisition rates to the multi-kHz regime needs to address two principle challenges: (i) finding an approach to increase the scan rates; (ii) precisely calibrating the delay axis of each individual scan.

Ultra-rapid delay-scanning has already been demonstrated by use of acousto-optic devices [35] and of purely mechanical approaches such as with a fast-rotating mirror [36], rotary mirror array [37], resonant galvanometer scanners [38–41], polygonal mirror scanners [39,42,43], or an ultrasonic sonotrode [29,34]. Delay calibration has been implemented with interferometric techniques [29,34,40,41,44]. Applications including optical coherence tomography, high-speed Fourier-transform coherent anti-stokes Raman scattering spectroscopy [40], spectral microscopy [41,42], and probing of non-reproducible, fast processes with FTIR spectroscopy [29,34,36,38,39] and EOS-based field-sensitive spectroscopy [34] have been presented.

One of the most versatile and powerful approaches to delay scanning spectroscopies is the use of two separate laser oscillators with stationary [45–49] or modulated [50–52] repetition-frequency stabilization. Synchronizing the repetition rates of mode-locked lasers with attosecond-level timing jitter [53] has been demonstrated as far back as two decades ago. Dual-frequency comb EOS with a timing jitter of 80 attoseconds has previously been demonstrated with two fiber lasers [54] that have been optically phase-locked with a constant repetition frequency offset of 50 Hz. The scan range of 10 nanoseconds was determined by the repetition rate. Modulated electronic phase locks enable higher scan speeds over reduced delay ranges, flexibly adjustable from nanoseconds to picoseconds [51,52,55,56]. However, electronic phase detection reportedly suffers from multi-femtosecond timing jitter [57], which is comparable to the oscillation period of a mid-IR wave. Therefore, while being highly versatile, the use of this approach, referred to as electronically controlled optical sampling (ECOPS), has been restricted to long-wave terahertz spectroscopy [50,58]. Recently, ECOPS has been implemented using an electro-optic modulator with dual-frequency interferometric calibration, resulting in sub-fs timing precision, albeit at scan ranges limited to the sub-picosecond regime [55,56].

Here, we report a dual-oscillator approach for multi-kHz field-resolved IR spectroscopy of condensed-phase samples, suitable for scanning over multi-picosecond delay ranges, based on ECOPS-type frequency locking. We draw on the extreme reproducibility of narrowband IR reference waveforms generated by intra-pulse difference frequency generation (IPDFG) [17,59], combined with electro-optic detection. The approach, which we dubbed electro-optic delay tracking (EODT), offers a calibration of the delay of gate pulses with respect to the IR fields yielding, with post-processing, a delay axis with down to 2.5 attosecond precision. EODT is not limited to field-resolved infrared spectroscopy, but provides a general approach to extend high-precision dual-oscillator and frequency-comb spectroscopy techniques to measurements with picosecond delay ranges, as typical for samples in the condensed phase.

In a test experiment, we demonstrate the real-time capture of a liquid injection event with a timing resolution of 357 μs, detecting absorbance changes at the level of 0.8 mOD for dimethyl sulfone ($DMSO_2$) dissolved in water. We also demonstrate detection of the electric-field response of a human blood serum sample excited by a nearly octave-spanning mid-IR pulse without measurable contributions from technical noise.

2. EXPERIMENTAL CONCEPT

The experimental scheme for dual-oscillator mid-IR field-sensitive spectroscopy with EODT is shown in Fig. 1. A detailed description of the experimental setup is included in Supplement 1. The system is based on two frequency-synchronized, mode-locked near-IR lasers (Laser 1 and Laser 2). Laser 1 drives mid-IR generation via IPDFG [14,60,61]. The resulting mid-IR pulses coherently excite a sample that emits a sample-specific electric field in the wake of the excitation [17,54]. EOS measures the excitation-pulse waveform and the sample response, both of which are convoluted with the instrument response function.

EOS detection is gated by pulses from Laser 2. Any difference in repetition frequency between the mutually locked Lasers 1 and 2 leads to changes in the delay between mid-IR and gate pulses. We use this effect by applying a sinusoidal modulation of the frequency lock that causes a continuously oscillating forward/backward delay scan of the gate pulses across the mid-IR waveforms [51,52]. We configure the modulation depth and frequency to record multi-picosecond-long EOS traces at kHz rates.

Jitter of the frequency lock between the two oscillators introduces additional unwanted modulation of the delay between mid-IR waveforms and gate pulses. To overcome the limits of electronic control, we use another EOS channel to optically track the instantaneous delay between pulses from both lasers. To this end, we generate a narrowband mid-IR reference waveform spreading in time over the full multi-picosecond delay range and sample it with a second EOS detection, gated with a replica of the gate pulse generated by Laser 2. The evolution of the electric-field oscillations of the mid-IR reference waveform in the laboratory time-frame is defined by its optical frequency and phase. The frequency is consistently defined over the entire delay range by the narrowband filter (described in the following section). The phase of the mid-IR reference waveform is reproducible from pulse to pulse due to the intrinsic phase-stability of IPDFG [59]. We use the known carrier frequency of the mid-IR reference wave to retrieve the delay axis for the sample EOS channel [34]. An active frequency lock synchronizes the 37th harmonic of the pulse-repetition frequency of Laser 2 to the 74th harmonic of Laser 1. We temporally scan across the mid-IR waveform with the gate pulse by modulating the frequency lock sinusoidally at 1.4 kHz. Thus, by scanning back and forth, 2800 EOS scans are recorded per second.

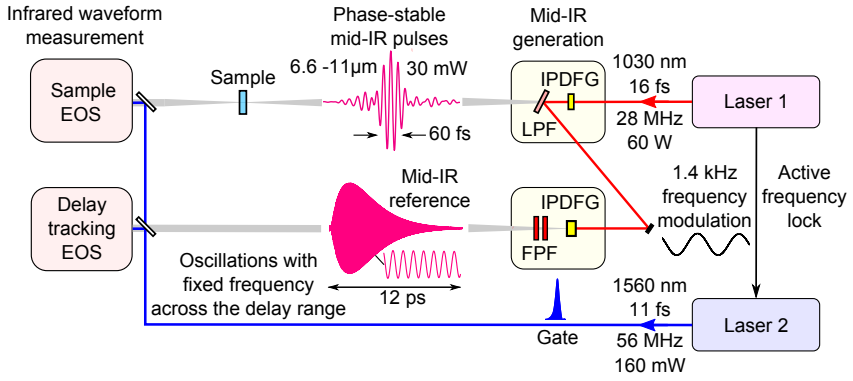

Fig. 1. Simplified experimental scheme for field-resolved mid-infrared measurements with two frequency-synchronized lasers with electro-optic delay tracking (EODT). The system layout is shown from right to left to maintain temporal causality in the shown waveforms. Laser 1 produces short mid-IR pulses for the sample measurements by intra-pulse difference frequency generation (IPDFG) in a $LiGaS_2$ crystal. The mid-IR electric field waveforms are measured with EOS, gated by ultrashort, 11-fs pulses from Laser 2. Laser 2 is actively frequency-synchronized to Laser 1. Modulating the frequency lock at 1.4 kHz facilitates rapid delay scanning. Jitter of the frequency lock translates into imprecision of the delay axis in the EOS measurement. The delay axis is calibrated through the EOS measurement of a narrowband, mid-IR reference wave covering the full delay range up to 12 ps, with a fixed oscillation period. It is generated by IPDFG in another $LiGaS_2$ crystal, followed by two custom-designed Fabry–Perot-type filters (FPF). LPF: low-pass filter.

3. RESULTS

A. Electro-Optic Delay Tracking (EODT)

For generating a reproducible reference waveform for delay tracking, we use spectral filtering with a sequence of two identical custom-designed, narrowband Fabry–Perot-type filters [62]. In Fig. 2(a), the top panel shows the transmittance (solid red line) and group delay on reflectance (solid blue line) of the filter, featuring single narrow peaks centered around 8.33 μm (1200 cm^{-1}). Transmittance data in the mid-IR range was measured using a Fourier transform IR spectrometer (Vertex 70, Bruker Optics GmbH) with a maximum resolution of 0.5 cm^{-1}. The group delay on reflectance (GDr) was extracted from the data recorded by a mid-IR white-light interferometer developed in-house [63]. The experimental transmittance and GDr shown in the bottom panel reproduce the shapes of the design curves, with slightly shifted maxima at 8.53 μm (1170 cm^{-1}) and a full width at half-maximum of only 48 nm (6.6 cm^{-1}). The 2% shift of the experimental curves with respect to the theoretical ones is caused

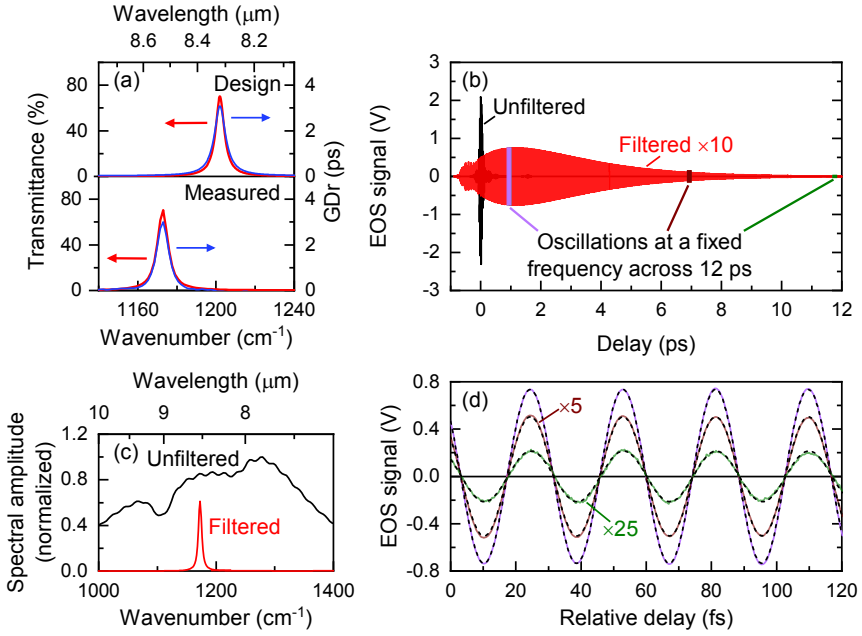

Fig. 2. Generation of the mid-IR reference pulse with a Fabry–Perot-type filters. (a) Theoretical spectral characteristics according to the design (top panel) and the corresponding experimental results (bottom panel) for transmittance and group delay on reflection (GDr) for the custom designed Fabry–Perot-type filters. (b) Comparison of time-domain EOS measurements of a broadband, unfiltered mid-IR waveform (black) and a long-lasting narrowband mid-IR waveform, obtained by placing two Fabry–Perot-type filters in the mid-IR beam path. (c) Experimental spectra corresponding to the unfiltered broadband (black) and filtered narrowband (red) mid-IR pulses. (d) Three sections of the filtered waveform in (b), marked by different colors, are zoomed and overlaid, demonstrating the stable frequency of oscillation for the filtered waveform across the entire delay range, covering 12 ps. A sine wave with a frequency of 35.2 THz and an amplitude that scales with the envelope of the filtered narrowband mid-IR waveform (black, dashed) overlap perfectly with the filtered waveform over all three intervals, demonstrating that the waveform has a constant frequency and phase.

by a slight variation in layer thickness that occurred during the deposition process.

Figure 2(b) shows the effect of the filters on the EOS waveform of a few-cycle mid-IR pulse, recorded independently with an instrument employing conventional mechanical scanning [17] with high-precision interferometric delay calibration [64]. Spectral filtering stretches the original 85-fs-long mid-IR waveform (black) over a ca. 12 ps long delay range (red). The unfiltered and filtered spectra are represented in the frequency domain in Fig. 2(c). Compared to other methods of temporally expanding the pulse, spectral filtering to a narrow band removes the influence of spectral distortion and frequency-dependent phase fluctuations on the signal shape.

The consistency of the waveform oscillations over the delay range is depicted in Fig. 2(d). We overlaid three 120-fs-long sections of the narrowband EOS trace of the filtered mid-IR waveform (purple, burgundy, and green) in order to compare them with the corresponding sections of a sinusoidal wave (dashed black), oscillating at a fixed frequency of 35.2 THz, with a constant phase, and an amplitude that follows the envelope of the narrowband EOS trace. The waveform sections oscillate in synchrony with the sine wave, indicating that the filtered IR reference waveform for delay tracking oscillates at a fixed frequency, with a stable carrier-envelope phase. We estimate that the cumulative error in assuming a quasi-continuous-wave reference waveform is below 100 as over the full 12 ps delay range (see Supplement 1). In contrast to interferometric delay calibration [55,56], the EOS signal of the IR reference waveform is intrinsically independent of the carrier-envelope phases of the two laser oscillators.

The raw sample and delay-tracking EOS signals are shown for an exemplary section of the measurement in Fig. 3(a). The modulated laser frequency lock performs recurring forward and backward scans over both waveforms. The green dots represent the turning points (TP1 and TP2), at which the direction of the delay scan changes. A single scan is acquired within 357 μs and comprises almost 10,000 data points. The data acquisition is synchronized with the arrival time of the individual laser pulses.

A single forward scan of the delay-tracking EOS signal is shown in Fig. 3(b), corresponding to a section between two consecutive turning points, TP1 and TP2. The oscillating delay axis leads to a variation of the delay step, with the largest delay steps between two data points in the center of the trace and the smallest delay steps at the ends. As a result, shown on a data index axis, the measured delay calibration trace (blue) exhibits a varying oscillation frequency [see also magnified insets in Fig. 3(b)]. The delay-tracking EOS signal serves as the input for the optical delay extraction (see Supplement 1). The delay axis is extracted by segmented fitting of a sinusoidal function to the oscillations of the mid-IR reference waveform.

The extracted delay axis is depicted in Fig. 3(c) and covers a range of ∼6 ps. It can be readily extended, limited only by (i) the duration of the IR reference waveform, defined by the width of the optical filter, along with the signal-to-noise ratio of the delay-tracking EOS, and (ii) the maximum sampling rate to resolve the carrier oscillations at a given pulse repetition frequency. In this work, the delay extraction was performed in post-processing. For demonstrating the consistency of our delay extraction with the original signal, we simulated the delay tracking EOS signal [red

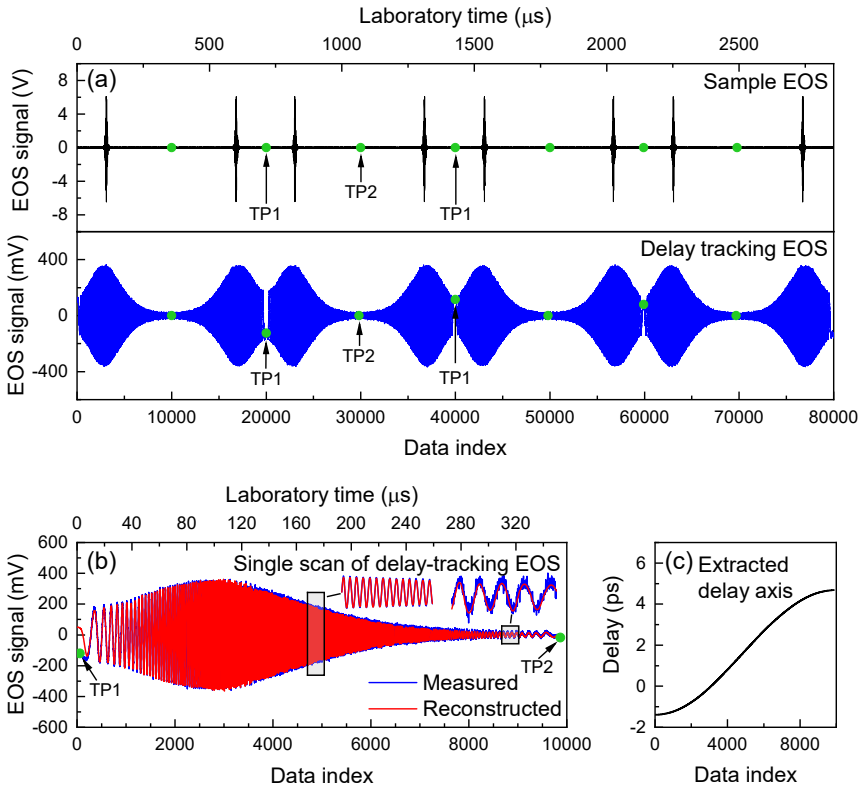

Fig. 3. Electro-optic delay tracking. (a) Continuous single-shot acquisition of sample (top panel) and delay tracking (bottom panel) EOS traces at a rate of 2800 scans per second, with each data point representing a single laser shot. The light green dots denote turning points of the delay scans. (b) Single scan of the delay tracking EOS signal (blue), between two adjacent turning points. The fixed carrier frequency and measured envelope of the delay-tracking EOS signal, along with the known relative frequency modulation that we apply between the repetition rates of the two lasers, enable the extraction of the delay axis and the reconstruction of the delay tracking signal (red). (c) Delay axis extracted from the delay-tracking EOS signal.

in Fig. 3(b)] as an oscillation with a constant carrier frequency on our delay axis, multiplied by a time-dependent envelope from the segmental fit. The insets in Fig. 3(b) show, for two magnified sections, that the reconstructed trace reproduces the measured data within the limits of experimental noise.

B. Detection Sensitivity and Dynamic Range

We showcase the sensitivity of our spectrometer and its ability to resolve the molecular response using a 1-mg/mL aqueous solution of dimethyl sulfone ($DMSO_2$) as a test sample. $DMSO_2$ has narrow IR absorption bands around 1140 cm^{-1} and 1290 cm^{-1}, corresponding to symmetric and asymmetric stretching vibrations of SO_2 [65,66]. Delay-corrected EOS measurements of a 1-mg/mL aqueous solution of $DMSO_2$ are depicted in Fig. 4(a). Already, a single trace (black), recorded within 357 μs, captures the EOS signal of the mid-IR waveform with a ratio between the peak signal and the standard deviation of the detection noise of 2840.

Due to technical limitations in detection brought about by the high radio-frequency bandwidth and high dynamic range required, we used two balanced photodetectors to capture the sample EOS signals: one optimized for strong signals and one for weak signals (see Supplement 1). The additional EOS channel for EODT employed a single detector. Note that each individual data point corresponds to a signal acquired with a single gate and mid-IR pulse pair.

Delay calibration with EODT allows us to directly overlay and average subsequent measurements in the time domain. The black trace in Fig. 4(a) shows the average over 560,000 EOS traces, corresponding to 200 s of acquisition time. It reproduces the waveform from the single measurement, with the only observable difference being a reduction in noise, best seen in the magnified section of the signal before the waveform. The magnified inset on the right shows the molecular response of $DMSO_2$, in the wake of the strong excitation pulse. Figure 4(b) shows Fourier transforms of the traces in Fig. 4(a), with the dashed lines corresponding to the detection noise floors, measured without any mid-IR pulses. The mid-IR pulses cover a spectral range of 6.6–11.0 μm (−20-dB intensity level), with a plateau between 7.5 and 9.7 μm. Field-sensitive detection, along with the brevity of the excitation pulses, enables temporal separation of the resonant molecular response from the excitation pulse. As a result, the large broadband background and the associated noise can be effectively removed, as will be described in the following section.

The spectral amplitude dynamic range, i.e., the ratio of the maximum spectral amplitude to the root-mean-square detection noise, increases statistically with the number of traces averaged

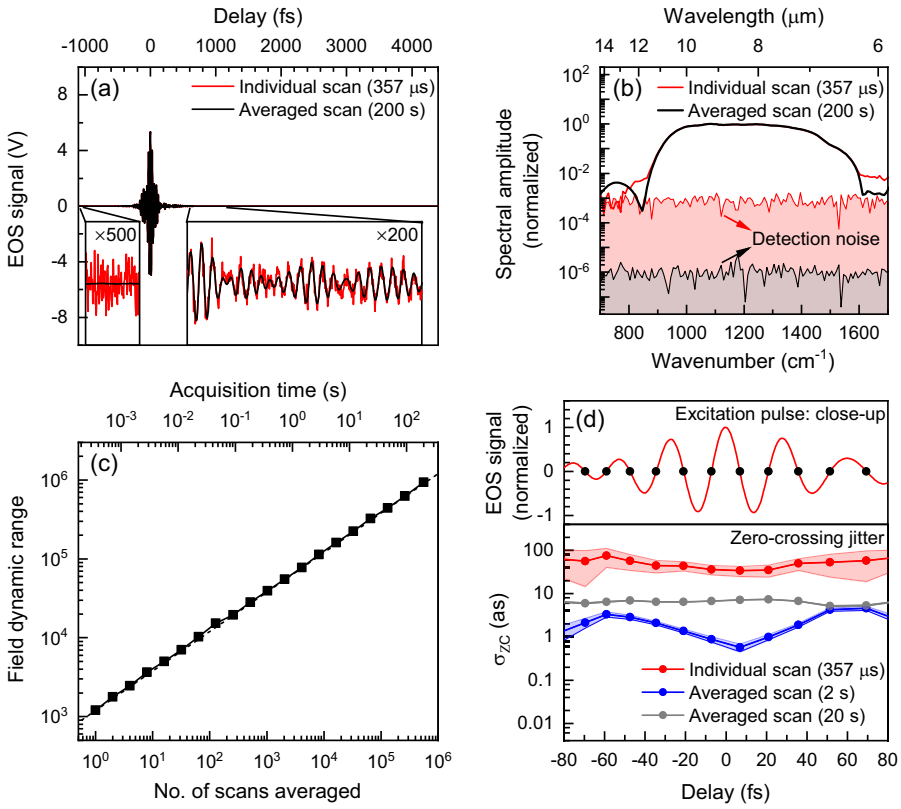

Fig. 4. Timing precision and dynamic range of delay-corrected electric field measurements. (a) Single-scan measurement of aqueous $DMSO_2$ solution, acquired in 357 μs (red) and average of 560,000 scans, which corresponds to 200 seconds of acquisition time (black). A zoom-in of a window temporally preceding the excitation pulse (left inset) shows the noise level for single (red) and averaged scans (black). The inset on the right shows the signal oscillations of the mid-IR waveform in the temporal region containing the impulsive excitation. (b) Fourier transform of the individual-scan (red solid line) and averaged-scan (black solid line) waveforms shown in (a). The shaded regions show the detection noise levels, corresponding to the individual-scan (red) and averaged-scan (black) waveforms shown in (a). (c) Spectral field amplitude dynamic range as a function of the number of scans averaged. (d) The top panel shows a close-up of the mid-IR reference waveform (red line) and the zero-crossing points (solid black circles). The standard deviation in the position of zero-crossing points (σ_{zc}) on comparing 20 consecutive individual scan (red) waveforms and averaged waveforms for averaging times of 2 s (blue) and 20 s (gray) are plotted in the bottom panel. The red and blue shaded regions show the uncertainty in the extracted timing precision, due to the detection noise (not to be confused with statistical error bars). The uncertainty corridor is not visible for the gray curve.

from 1200 for a single trace to 9.37×10^5 for all 560,000 EOS averaged traces. As demonstrated in Fig. 4(c), we find a linear increase of the field dynamic range, with the square root of the measurement time. With a slope of $6.62 \times 10^4\ s^{-1/2}$, the relationship is consistent with statistical noise behavior over 200 s of continuous measurement. With our approach, the sensitivity of dual-oscillator field-resolved IR spectroscopy thus increases strictly with measurement time, without any apparent signal deterioration on the time scales we studied.

The reproducibility of the measured waveforms, after applying the calibration of the delay axis with EODT, is further studied in Fig. 4(d). The top panel shows a close-up of the strong excitation-pulse signal of a single measurement trace. The slope of the waveform, and thus the sensitivity to variations of the waveform phase and of the delay axis, is highest at the zero-crossings of the signal, indicated by black dots. We quantify the temporal reproducibility of the waveform by calculating the standard deviations of the zero-crossing positions [bottom panel of Fig. 4(d)]. For 20 consecutive single scans with 357 μs acquisition time each (red), we find a standard deviation of 50 attoseconds (as) as the mean value of the 11 zero crossings in the displayed delay region from −80 fs to + 80 fs, containing the strong excitation pulse. The shaded region represents the uncertainty in determining the positions of the zero-crossings, due to the detection noise. On analyzing 20 consecutive averaged traces, each acquired in 2 s (blue), we find a standard deviation of 2.5 as, corresponding to a phase change of 0.6 mrad at the carrier wavelength of 8.2 μm.

On further averaging of scans, considering 20 s of acquisition for each averaged trace (gray), the standard deviation in the zero-crossing position increases to 6.5 as. The reduced detection noise at this level of averaging, combined with the fact that the y-axis follows a logarithmic scale, makes the uncertainty corridor hardly visible for the gray plot representing the 20 s averaged scans. The total measurement time for the 20 traces evaluated for calculating the standard deviation is 400 s, leading to effects of slow fluctuations on the minute-time-scale affecting the stability of measurements.

The best previously reported ECOPS results were, to our knowledge, based on picosecond-range scanning with an electro-optic modulation, reaching ∼86 as in 30 ms of acquisition [56]. Our 2.5 attosecond timing precision obtained with EODT exceeds what has been achieved with interferometric delay tracking techniques in a slow delay scanning approach [17] by a factor of 4 and is similar to that shown previously by a rapid mechanical delay scanning approach with an ultrasonic sonotrode [34]. The excellent reproducibility achieved with EODT-based delay calibration renders kHz-rate dual-oscillator EOS with multi-picosecond delay ranges suitable both for high-speed IR monitoring of fast processes and reactions, and for sensitive spectroscopy with longer acquisition times, spanning multiple seconds.

C. Reproducibility of the Sample-Specific Molecular Fingerprint

The absorption spectra of bio-fluids such as blood serum or plasma portray a combined effect of the vast variety of molecular constituents that make up the sample. The depth of information that can be extracted is linked to the sensitivity and reproducibility of the measurements.

To assess the spectroscopic performance for real-life biological samples, we characterized the noise properties of the resonant response of human blood serum to a broadband, impulsive excitation. A measurement of pure water was used as the reference. The reproducibility of the sample response was evaluated both in the time domain and in the frequency domain. For this measurement, 16,400 traces were averaged for each of the reference and sample measurements. The signal envelopes of the sample and reference waveforms are plotted in black and blue in Fig. 5(a). The signals are normalized to the peak of the excitation pulse. On subtracting an averaged EOS trace of the reference from the sample, we obtain a signal representing the difference in the temporal response of serum and of water (red). This is the sample-specific molecular fingerprint, including solvation. The detection noise of our EOS scheme, quantified by blocking the mid-IR beam, is plotted in gray.

Figure 5(b) shows the relative standard deviation of the normalized EOS traces with human blood serum in the liquid cuvette, as a function of optical delay, averaging 16,400 scans (black). The calculated gate-pulse shot-noise is plotted as a dashed line. The standard deviation drops to the gate-pulse shot-noise level 600 fs after the peak of the excitation. We apply a high-pass time-domain filter starting at this delay point, as will be described below. This is denoted by the green dashed vertical line in Fig. 5(b).

Furthermore, we analyzed the spectral reproducibility of the sample response in the frequency domain. The sample response of human blood serum for the case with no averaging (single reference and sample trace) is plotted in gray in Fig. 5(c). The standard deviation is marked by the gray shaded region. When performing the analysis on the full signal, low-frequency variations of the main excitation pulse can overwhelm small sample-response signals. Field-sensitive detection allows us to temporally separate the excitation and the resonant sample response, which carries most of the sample-specific information [17,18], to a large extent. This feature can also be exploited in the processing of the acquired sample spectrum. By applying a time-domain filter to the sample response [19,20], 600 fs after the peak of the excitation, the noise carried by the strong excitation can be largely suppressed.

The green plot in Fig. 5(c) represents a time-domain filtered sample response normalized to its peak value, along with its standard deviation. The time-domain high-pass filter removes inter-measurement fluctuations of the baseline at the expense of altering the spectral appearance of the signal. The oscillations are the result of the filter emphasizing sharp spectral features, and of the sharp cut-on of the Heaviside step function applied in the time-domain.

In addition, the reproducibility is quantified in terms of the Allan deviation in Fig. 5(d). The wavenumber-averaged Allan deviation of the sample-response (gray) decreases with the square root of the number of scans averaged up to 64 scans, before deviating from the trend. We assign the onset of deviations at 64 traces averaging (around 20 ms of acquisition time) to the influence of mechanical drifts and low-frequency electronic noise on the measurement. Time-domain filtering restores the square-root dependence of the residual noise for acquisition times of up to 6 s, as shown by the green plot. For this measurement, with an acquisition time of 200 s, we plotted the Allan deviation for averaging times up to ∼6 s, ensuring a sufficient number of sample segments for statistics. The Allan deviation of the time-domain filtered sample response is at the level of the calculated gate-pulse shot-noise, represented by the dashed black line in Fig. 5(d) (see Supplement 1 for the determination of the gate-pulse shot-noise level).

A major part of the absorption in human blood serum is attributed to proteins and their structural modifications. The current

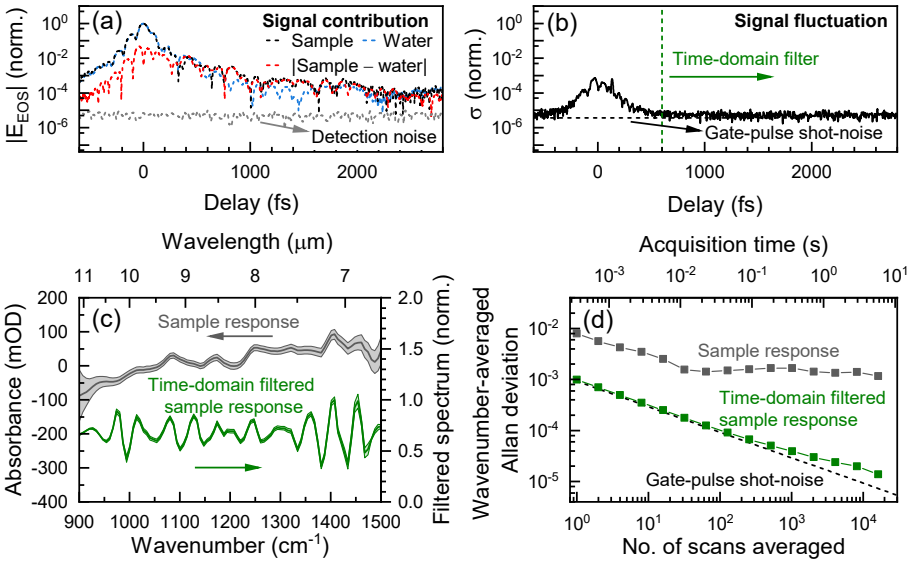

Fig. 5. Molecular response and noise characteristics in time and frequency domains. (a) Signal contributions: Envelopes of EOS measurements ($|E_{EOS}|$) with human blood serum and water in the liquid cuvette, averaging 16,400 scans, normalized to the peak signal of the excitation pulse (black and blue) and the envelope of the difference of the two EOS signals corresponding to the sample-specific fingerprint (red). The detection noise, averaging 16,400 scans, is plotted in gray. Laser intensity fluctuations between subsequent sample measurements render it difficult to accurately normalize the time-domain traces. We counter this challenge by time-domain filtering. (b) Signal fluctuations: the standard deviation across traces for 16,400-averaged scans normalized to the peak of the excitation-pulse signal is plotted in black. The dashed line shows the calculated near-IR shot noise. The green vertical dashed line indicates the onset of a high-pass time-domain filter [19] opening at 600 fs. (c) Sample response of blood serum, and its standard deviation, for a single-scan measurement of the reference and the sample (gray solid line and shaded region). By applying a time-domain filter, the relative noise can be significantly reduced (green line and shaded region). (d) Allan deviations, averaged over all wavenumbers, of the unfiltered (gray) as well as the time-domain filtered (green) sample response, compared to the gate-pulse shot-noise (black, dashed).

instrument covers the amide III band ranging from 1250 cm^{-1} to 1350 cm^{-1}, which is sensitive to the secondary structure of proteins, and is only mildly affected by absorption in water [67]. The region between 1000 cm^{-1} and 1180 cm^{-1} reveals signatures of protein glycosylation [68] and a significant post-translational modification linked to an individual's health state [69], as well as that of metabolites such as glucose. Though the complex molecular fingerprint cannot be fully traced back to the constituent molecules, patterns in the spectral shape provide information that is relevant for disease detection [2].

D. Spectroscopy of Fluids in Motion

Finally, we characterized the ability of the instrument to measure fast, dynamic events. $DMSO_2$ was again employed as a test sample and injected into the previously water-filled cuvette. We measured the evolving spectrum of the liquid in the cuvette by recording individual EOS scans with 357 μs acquisition time each, corresponding to an acquisition rate of 2.8 kHz.

The 2D heatmap in Fig. 6 describes the injection event, following the mid-IR absorbance dynamics in the spectral domain in the band from 1000 cm^{-1} to 1440 cm^{-1}. After Fourier-transforming the individual traces, we removed the slowly varying spectral backgrounds by applying a 4th-order polynomial baseline correction algorithm [70]. The spectral amplitude and phase at the initial (0 s) and final (4.4 s) points of the injection event are plotted to the right of the heatmap, in black and red, respectively. The red plots thus represent aqueous $DMSO_2$ solution.

To obtain a clearer picture of the dynamics, we take sections of the heatmap at the maxima of the $DMSO_2$ absorption bands at 1140 cm^{-1} and 1290 cm^{-1}, as shown by the dashed horizontal lines in the bottom panel. The absorbance corresponding to the two spectral components have been plotted in burgundy and light red. The two absorption peaks have a similar amplitude, with the absorbance reaching 16 and 18 mOD. We determined the standard deviation in absorbance to be 0.8 and 1.1 mOD for the lines at 1140 cm^{-1} and 1290 cm^{-1}, respectively. The standard deviation was calculated over the first 100 ms, where the value of absorbance is stable.

At sub-millisecond timing resolution, our absorption sensitivity reaches a performance achievable with quantum-cascade-laser-based spectroscopy, and applied, e.g., in the past for studying the dynamics of protein reactions [27], combustion dynamics [26], and electrochemical reactions [28]. However, our field-sensitive IR spectrometer features nearly octave-spanning mid-IR coverage—up to an order of magnitude more than what has been demonstrated with quantum cascade lasers. Together with the capabilities to measure both amplitude and phase spectra of the mid-IR waveforms with high sensitivity [17], as well as to investigate thick, strongly absorbing samples [17], dual-oscillator field-sensitive IR spectroscopy holds promise for becoming a versatile tool for monitoring rapid dynamics.

4. CONCLUSION

In conclusion, we presented a dual-oscillator-based spectrometer, performing field-resolved mid-infrared (mid-IR) measurements with electro-optic sampling (EOS) at 2800 scans per second. The instrument records highly reproducible mid-IR waveforms by using electro-optic delay tracking (EODT) as a new technique to calibrate the delay axis of each scan. The delay calibration allows consistent, ultra-rapid measurements of mid-IR EOS traces, and

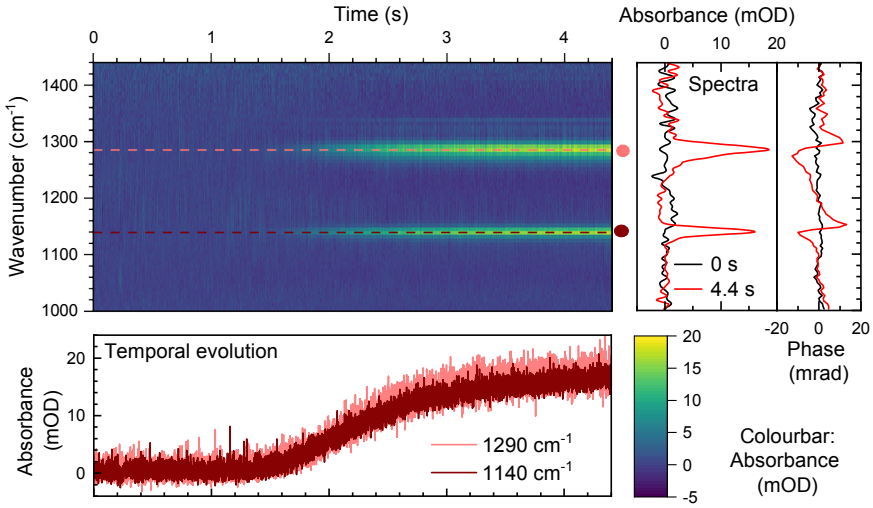

Fig. 6. Spectral dynamics of fluid injection with sub-millisecond timing resolution. Temporal evolution of absorbance for spectral components from 1000 to 1440 cm^{-1}, during the injection of an aqueous 1 mg/ml $DMSO_2$ solution into the sample cuvette that initially contained water (2D heatmap). Both the absorbance and the phase for individual spectra with 357 µs acquisition time taken before (0 s) and after (4.4 s) injection are plotted in the right panel. The evolution of absorbance at the two $DMSO_2$ absorption bands at 1140 cm^{-1} and 1290 cm^{-1} bands are shown in the bottom panel.

direct time-domain averaging over minutes of acquisition, with the field dynamic range increasing with the square root of the measurement time for temporally filtered molecular signals. From an analysis of the zero-crossings of the measured mid-IR waveforms, we found a timing precision of 50 attoseconds for single 357-µs-long scans, improving towards the 2.5 attosecond frontier for 2 s of averaging. The infrared fingerprint of human blood serum could be detected at the shot-noise limit of the gate pulses 600 fs after the excitation-pulse peak.

The ultra-rapid mid-IR EOS detection system presented here combines the sensitivity of field-resolved detection with the flexibility of dual-oscillator scanning at multi-kHz scan rates, while reaching attosecond timing precision and reproducibility of the recorded waveforms. Possible applications harnessing the high speed of the method range from the real-time tracking of reaction dynamics [26–28] to label-free flow-cytometry [31–33]. The advantage of measuring the resonant response of molecular samples to coherent optical excitation in a field-sensitive manner with a broad spectral coverage, and in the absence of technical noise contributions, gives the system a unique place at the forefront of infrared spectroscopy development for samples in the condensed phase. The high timing precision and intrinsic waveform stability render the technique promising for extension towards mid-infrared frequency-comb spectroscopy. Furthermore, dual-oscillator scanning with high-precision delay calibration via EODT is also directly compatible with many nonlinear spectroscopies, such as pump-probe, coherent anti-Stokes Raman, and photon echo spectroscopies—especially those which do not require carrier-envelope phase stabilization of the driving sources.

Funding. Deutsche Forschungsgemeinschaft (EXC 2051, 390713860); Centre for Advanced Laser Applications; Max Planck School of Photonics; Max-Planck-Institut für Quantenoptik.

Acknowledgment. This work was funded by the Deutsche Forschungsgemeinschaft (DFG, German Research Foundation) under Germany's Excellence Strategy - EXC 2051 - Project-ID 390713860, Center for Molecular Fingerprinting (CMF), State Research Center OPTIMAS, Max Planck Technology Transfer Program, and the International Max Planck Research School on Advanced Photon Science (IMPRS – APS).

Disclosures. The authors declare no conflicts of interests.

Data availability. Data underlying the results presented in this paper are not publicly available at this time but may be obtained from the authors upon reasonable request.

Supplemental document. See Supplement 1 for supporting content.

REFERENCES

1. J. Backhaus, R. Mueller, N. Formanski, *et al.*, "Diagnosis of breast cancer with infrared spectroscopy from serum samples," Vib. Spectrosc. **52**, 173–177 (2010).
2. M. Huber, K. V. Kepesidis, L. Voronina, *et al.*, "Infrared molecular fingerprinting of blood-based liquid biopsies for the detection of cancer," eLife **10**, e68758 (2021).
3. K. M. G. Lima, K. B. Gajjar, P. L. Martin-Hirsch, *et al.*, "Segregation of ovarian cancer stage exploiting spectral biomarkers derived from blood plasma or serum analysis: ATR-FTIR spectroscopy coupled with variable selection methods," Biotechnol. Prog. **31**, 832–839 (2015).
4. D. Sheng, X. Liu, W. Li, *et al.*, "Distinction of leukemia patients' and healthy persons' serum using FTIR spectroscopy," Spectrochim. Acta A **101**, 228–232 (2013).
5. M. Paraskevaidi, C. L. M. Morais, K. M. G. Lima, *et al.*, "Potential of mid-infrared spectroscopy as a non-invasive diagnostic test in urine for endometrial or ovarian cancer," Analyst **143**, 3156–3163 (2018).
6. V. Untereiner, G. D. Sockalingum, R. Garnotel, *et al.*, "Bile analysis using high-throughput FTIR spectroscopy for the diagnosis of malignant biliary strictures: a pilot study in 57 patients," J. Biophoton. **7**, 241–253 (2014).
7. P. D. Lewis, K. E. Lewis, R. Ghosal, *et al.*, "Evaluation of FTIR Spectroscopy as a diagnostic tool for lung cancer using sputum," BMC Cancer **10**, 640 (2010).
8. G. E. Menzies, H. R. Fox, C. Marnane, *et al.*, "Fourier transform infrared for noninvasive optical diagnosis of oral, oropharyngeal, and laryngeal cancer," Transl. Res. **163**, 19–26 (2014).
9. I. Maitra, C. L. M. Morais, K. M. G. Lima, *et al.*, "Attenuated total reflection Fourier-transform infrared spectral discrimination in human bodily fluids of oesophageal transformation to adenocarcinoma," Analyst **144**, 7447–7456 (2019).
10. M. Sánchez-Brito, F. J. Luna-Rosas, R. Mendoza-González, *et al.*, "A machine-learning strategy to evaluate the use of FTIR spectra of saliva for a good control of type 2 diabetes," Talanta **221**, 121650 (2021).
11. K. S. Maiti, E. Fill, F. Strittmatter, *et al.*, "Towards reliable diagnostics of prostate cancer via breath," Sci. Rep. **11**, 18381 (2021).

12. M. Huber, K. V. Kepesidis, L. Voronina, *et al.*, "Stability of person-specific blood-based infrared molecular fingerprints opens up prospects for health monitoring," Nat. Commun. **12**, 1511 (2021).
13. M. J. Baker, S. R. Hussain, L. Lovergne, *et al.*, "Developing and understanding biofluid vibrational spectroscopy: a critical review," Chem. Soc. Rev. **45**, 1803–1818 (2016).
14. I. Pupeza, D. Sánchez, J. Zhang, *et al.*, "High-power sub-two-cycle mid-infrared pulses at 100 MHz repetition rate," Nat. Photonics **9**, 721–724 (2015).
15. P. Steinleitner, N. Nagl, M. Kowalczyk, *et al.*, "Single-cycle infrared waveform control," Nat. Photonics **16**, 512–518 (2022).
16. C. Hofer, D. Gerz, M. Högner, *et al.*, "Mid-infrared electric field sampling approaching single-photon sensitivity," EPJ Web Conf. **243**, 16001 (2020).
17. I. Pupeza, M. Huber, M. Trubetskov, *et al.*, "Field-resolved infrared spectroscopy of biological systems," Nature **577**, 52–59 (2020).
18. M. T. Peschel, M. Högner, T. Buberl, *et al.*, "Sub-optical-cycle light-matter energy transfer in molecular vibrational spectroscopy," Nat. Commun. **13**, 5897 (2022).
19. M. Huber, M. Trubetskov, W. Schweinberger, *et al.*, "Standardised electric-field-resolved molecular fingerprinting," Anal. Chem., submitted for publication.
20. M. Huber, M. Trubetskov, W. Schweinberger, *et al.*, "Standardising electric-field-resolved molecular fingerprints," in *Conference on Lasers and Electro-Optics Europe and European Quantum Electronics Conference* (2023).
21. M. Huber, M. Trubetskov, S. A. Hussain, *et al.*, "Optimum sample thickness for trace analyte detection with field-resolved infrared spectroscopy," Anal. Chem. **92**, 7508–7514 (2020).
22. C. Kübler, R. Huber, S. Tübel, *et al.*, "Ultrabroadband detection of multi-terahertz field transients with GaSe electro-optic sensors: approaching the near infrared," Appl. Phys. Lett. **85**, 3360–3362 (2004).
23. A. Leitenstorfer, S. Hunsche, J. Shah, *et al.*, "Detectors and sources for ultrabroadband electro-optic sampling: experiment and theory," Appl. Phys. Lett. **74**, 1516–1518 (1999).
24. J. Valdmanis and G. Mourou, "Subpicosecond electrooptic sampling: principles and applications," IEEE J. Quantum Electron. **22**, 69–78 (1986).
25. Q. Wu and X. C. Zhang, "Free-space electro-optic sampling of terahertz beams," Appl. Phys. Lett. **67**, 3523–3525 (1995).
26. N. H. Pinkowski, Y. Ding, C. L. Strand, *et al.*, "Dual-comb spectroscopy for high-temperature reaction kinetics," Meas. Sci. Technol. **31**, 055501 (2020).
27. J. L. Klocke, M. Mangold, P. Allmendinger, *et al.*, "Single-shot sub-microsecond mid-infrared spectroscopy on protein reactions with quantum cascade laser frequency combs," Anal. Chem. **90**, 10494–10500 (2018).
28. E. Lins, S. Read, B. Unni, *et al.*, "Microsecond resolved infrared spectroelectrochemistry using dual frequency comb IR lasers," Anal. Chem. **92**, 6241–6244 (2020).
29. B. Süss, F. Ringleb, and J. Heberle, "New ultrarapid-scanning interferometer for FT-IR spectroscopy with microsecond time-resolution," Rev. Sci. Instrum. **87**, 063113 (2016).
30. R. Ghorbani and F. M. Schmidt, "Real-time breath gas analysis of CO and CO_2 using an EC-QCL," Appl. Phys. B **123**, 144 (2017).
31. D. Gerz, M. Huber, H. Mirkes, *et al.*, "High-speed field-resolved infrared fingerprinting of particles in flow," in *Conference on Lasers and Electro-Optics Europe and European Quantum Electronics Conference* (Optica Publishing Group, 2023), paper cl_2_1.
32. K. Hiramatsu, T. Ideguchi, Y. Yonamine, *et al.*, "High-throughput label-free molecular fingerprinting flow cytometry," Sci. Adv. **5**, eaau0241 (2019).
33. Y. Suzuki, K. Kobayashi, Y. Wakisaka, *et al.*, "Label-free chemical imaging flow cytometry by high-speed multicolor stimulated Raman scattering," Proc. Natl. Acad. Sci. USA **116**, 15842–15848 (2019).
34. A. Weigel, P. Jacob, D. Gröters, *et al.*, "Ultra-rapid electro-optic sampling of octave-spanning mid-infrared waveforms," Opt. Express **29**, 20747–20764 (2021).
35. O. Schubert, M. Eisele, V. Crozatier, *et al.*, "Rapid-scan acousto-optical delay line with 34 kHz scan rate and 15 as precision," Opt. Lett. **38**, 2907–2910 (2013).
36. P. R. Griffiths, B. L. Hirsche, and C. J. Manning, "Ultra-rapid-scanning Fourier transform infrared spectrometry," Vib. Spectrosc. **19**, 165–176 (1999).
37. N. G. Chen and Q. Zhu, "Rotary mirror array for high-speed optical coherence tomography," Opt. Lett. **27**, 607–609 (2002).
38. K. Hashimoto, V. R. Badarla, and T. Ideguchi, "High-speed Fourier-transform infrared spectroscopy with phase-controlled delay line," Laser Photon. Rev. **15**, 2000374 (2021).
39. K. Hashimoto and T. Ideguchi, "Phase-controlled Fourier-transform spectroscopy," Nat. Commun. **9**, 4448 (2018).
40. K. Hashimoto, M. Takahashi, T. Ideguchi, *et al.*, "Broadband coherent Raman spectroscopy running at 24,000 spectra per second," Sci. Rep. **6**, 21036 (2016).
41. R. Kinegawa, K. Hiramatsu, K. Hashimoto, *et al.*, "High-speed broadband Fourier-transform coherent anti-Stokes Raman scattering spectral microscopy," J. Raman Spectrosc. **50**, 1141–1146 (2019).
42. F. Sinjab, K. Hashimoto, V. R. Badarla, *et al.*, "Multimodal laser-scanning nonlinear optical microscope with a rapid broadband Fourier-transform coherent Raman modality," Opt. Express **28**, 20794–20807 (2020).
43. M. Tamamitsu, Y. Sakaki, T. Nakamura, *et al.*, "Ultrafast broadband Fourier-transform CARS spectroscopy at 50,000 spectra/s enabled by a scanning Fourier-domain delay line," Vib. Spectrosc. **91**, 163–169 (2017).
44. S. L. Camenzind, D. Koenen, B. Willenberg, *et al.*, "Timing jitter characterization of free-running dual-comb laser with sub-attosecond resolution using optical heterodyne detection," Opt. Express **30**, 5075–5094 (2022).
45. A. Bartels, F. Hudert, C. Janke, *et al.*, "Femtosecond time-resolved optical pump-probe spectroscopy at kilohertz-scan-rates over nanosecond-time-delays without mechanical delay line," Appl. Phys. Lett. **88**, 041117 (2006).
46. P. A. Elzinga, R. J. Kneisler, F. E. Lytle, *et al.*, "Pump/probe method for fast analysis of visible spectral signatures utilizing asynchronous optical sampling," Appl. Opt. **26**, 4303–4309 (1987).
47. O. Kliebisch, D. C. Heinecke, and T. Dekorsy, "Ultrafast time-domain spectroscopy system using 10 GHz asynchronous optical sampling with 100 kHz scan rate," Opt. Express **24**, 29930–29940 (2016).
48. T. Yasui, E. Saneyoshi, and T. Araki, "Asynchronous optical sampling terahertz time-domain spectroscopy for ultrahigh spectral resolution and rapid data acquisition," Appl. Phys. Lett. **87**, 061101 (2005).
49. R. Gebs, G. Klatt, C. Janke, *et al.*, "High-speed asynchronous optical sampling with sub-50fs time resolution," Opt. Express **18**, 5974–5983 (2010).
50. R. J. B. Dietz, N. Vieweg, T. Puppe, *et al.*, "All fiber-coupled THz-TDS system with kHz measurement rate based on electronically controlled optical sampling," Opt. Lett. **39**, 6482–6485 (2014).
51. S. Kray, F. Spöler, T. Hellerer, *et al.*, "Electronically controlled coherent linear optical sampling for optical coherence tomography," Opt. Express **18**, 9976–9990 (2010).
52. F. Tauser, C. Rausch, J. H. Posthumus, *et al.*, "Electronically controlled optical sampling using 100 MHz repetition rate fiber lasers," Proc. SPIE **6881**, 68810O (2008).
53. T. R. Schibli, J. Kim, O. Kuzucu, *et al.*, "Attosecond active synchronization of passively mode-locked lasers by balanced cross correlation," Opt. Lett. **28**, 947–949 (2003).
54. A. S. Kowligy, H. Timmers, A. J. Lind, *et al.*, "Infrared electric field sampled frequency comb spectroscopy," Sci. Adv. **5**, eaaw8794 (2019).
55. R. Kameyama, S. Takizawa, K. Hiramatsu, *et al.*, "Dual-comb coherent Raman spectroscopy with near 100% duty cycle," ACS Photon. **8**, 975–981 (2021).
56. Y. Shi, D. Hu, R. Xue, *et al.*, "High speed time-of-flight displacement measurement based on dual-comb electronically controlled optical sampling," Opt. Express **30**, 8391–8398 (2022).
57. F. Paries, O. Boidol, G. von Freymann, *et al.*, "Electronic phase detection with a sub-10 fs timing jitter for terahertz time-domain spectroscopy systems," Opt. Express **31**, 6027–6038 (2023).
58. Y. Kim and D.-S. Yee, "High-speed terahertz time-domain spectroscopy based on electronically controlled optical sampling," Opt. Lett. **35**, 3715–3717 (2010).
59. S. A. Hussain, W. Schweinberger, T. Buberl, *et al.*, "Train of ultrashort mid-infrared pulses with sub-mrad carrier-envelope phase stability," in *Conference on Lasers and Electro-Optics Europe and European Quantum Electronics Conference* (Optica Publishing Group, 2019), paper ed_6_2.
60. C. Gaida, M. Gebhardt, T. Heuermann, *et al.*, "Watt-scale super-octave mid-infrared intrapulse difference frequency generation," Light Sci. Appl. **7**, 94 (2018).

61. H. Fattahi, A. Schwarz, S. Keiber, *et al.*, "Efficient, octave-spanning difference-frequency generation using few-cycle pulses in simple collinear geometry," Opt. Lett. **38**, 4216–4219 (2013).
62. T. Amotchkina, M. Trubetskov, A. Weigel, *et al.*, "Fabry-Pérot based temporal standard at 8.5 μm for electro-optic delay tracking," in *Conference on Lasers and Electro-Optics Europe and European Quantum Electronics Conference* (Optica Publishing Group, 2021), paper ce_6_2.
63. F. Habel, M. Trubetskov, and V. Pervak, "Group delay dispersion measurements in the mid-infrared spectral range of 2–20 μm," Opt. Express **24**, 16705–16710 (2016).
64. W. Schweinberger, L. Vamos, J. Xu, *et al.*, "Interferometric delay tracking for low-noise Mach-Zehnder-type scanning measurements," Opt. Express **27**, 4789–4798 (2019).
65. W. R. Feairheller and J. E. Katon, "The vibrational spectra of sulfones," Spectrochim. Acta **20**, 1099–1108 (1964).
66. T. Uno, K. Machida, and K. Hanai, "Vibrational spectra of dimethyl sulphone and dimethyl sulphone-d6," Spectrochim. Acta A **27**, 107–118 (1971).
67. C. Stani, L. Vaccari, E. Mitri, *et al.*, "FTIR investigation of the secondary structure of type I collagen: new insight into the amide III band," Spectrochim. Acta A **229**, 118006 (2020).
68. M. Khajehpour, J. L. Dashnau, and J. M. Vanderkooi, "Infrared spectroscopy used to evaluate glycosylation of proteins," Anal. Biochem. **348**, 40–48 (2006).
69. L. Voronina, F. Fleischmann, J. Šimunović, *et al.*, "Probing blood plasma protein glycosylation with infrared spectroscopy," Anal. Chem. **96**, 2830–2839 (2024).
70. J. Zhao, H. Lui, D. I. McLean, *et al.*, "Automated autofluorescence background subtraction algorithm for biomedical Raman spectroscopy," Appl. Spectrosc. **61**, 1225–1232 (2007).